



Pathways towards managing cost and degradation risk of fast charging cells with electrical and thermal controls

Journal:	<i>Energy & Environmental Science</i>
Manuscript ID	EE-ART-07-2021-002286.R1
Article Type:	Paper
Date Submitted by the Author:	22-Oct-2021
Complete List of Authors:	<p>Song, Juhyun; Argonne National Laboratory, Chemical Sciences and Engineering Division Liu, Zhe; Argonne National Laboratory, Chemical Sciences and Engineering Division Knehr, Kevin; Argonne National Laboratory, Chemical Sciences and Engineering Division Kubal, Joseph; Argonne National Laboratory, Chemical Sciences and Engineering Division Kim, Hong-Keun; Argonne National Laboratory, Chemical Sciences and Engineering Division Dees, Dennis; Argonne National Laboratory, Chemical Sciences and Engineering Division Nelson, Paul; Argonne National Laboratory, Chemical Sciences and Engineering Division Ahmed, Shabbir; Argonne National Laboratory, Chemical Sciences and Engineering Division</p>

Pathways towards managing cost and degradation risk of fast charging cells with electrical and thermal controls

Juhyun Song^{†*}, Zhe Liu[†], Kevin W. Knehr^{*}, Joseph J. Kubal, Hong Keun Kim, Dennis W. Dees, Paul A. Nelson, Shabbir Ahmed

Abstract

The charging rate of Li-ion batteries is limited by the risks of lithium plating and thermal damage, both of which negatively affect lifetime of the batteries. This work analyzes how to minimize charge time and manage the risk of degradation using both electrical and thermal controls. To accomplish this, an electrochemical-thermal model is developed to introduce a constant-risk fast charging protocol which maximizes the charging current while maintaining the cell within pre-defined design limits selected to minimize the risk of degradation. Results indicate 80%-charging of a typical NMC/graphite cell can be achieved within 10 minutes with a cell cost under \$100/kWh (corresponding to an 80- μ m thick anode) when charged at moderate allowable risks of degradation. We also demonstrate how stretching the allowable risk (*i.e.*, higher temperatures, larger C-rates, and lower anode potential limits) allows affordable design of fast charging cells.

Chemical Science and Engineering Division; Argonne National Laboratory, Lemont, IL 60439, USA.

[†] These authors contributed equally

* Corresponding authors: jusong@apple.com (J.S.), knehrkw@anl.gov (K.W.K)

Electronic Supplementary Information (ESI) available: 14 Figures and 4 tables providing additional data and modeling details.

Introduction

Improving the fast charging capability of lithium-ion batteries is crucial to increase the widespread adoption of electric vehicles.¹ In particular, progress requires the development of battery packs that can charge a large portion of their capacity (~80%) on time scales similar to the refueling of an internal combustion engine vehicle (<15 minutes).²⁻⁴ Fast charging of lithium—ion batteries is done at high currents, which leads to increased heat generation and the potential for lithium plating in the battery.⁵⁻⁸ Both phenomena have been shown to increase degradation, which reduces cycle life and can increase safety risks.⁹⁻¹⁸

Colclasure et al. have illustrated that, for conventional cells with moderately loaded electrodes (~1.5 to ~2.5 mAh cm⁻² or ~30 to ~70- μ m thick), fast charging in <15 minutes using standard constant current methods will trigger significant lithium plating.¹⁹ Further work has shown this can be mitigated by restricting the state of charge during fast charging to ~40% of the cells' capacity, but it comes at a detriment to the range of the vehicle.²⁰ Thus, modifications to the cell design and operating conditions beyond conventional practices are required to enable fast charging.

Considerable work has been done on achieving fast charging without triggering degradation mechanisms. To achieve fast charging of the full usable capacity, several authors have outlined the need to reduce the cell impedance and improve the transport properties of lithium ions through the electrolyte and electrodes, which inhibits plating and reduces heat generation.^{19,21-26} This includes reducing the electrode thickness by decreasing the loading.² However, this increases the cost of the battery (\$/kWh) by increasing the amount of non-active materials (*i.e.*, current collectors and separators).

Besides modifying the cell, changes to the operating conditions have been proposed to achieve fast charging. For instance, increasing the temperature during charging improves the electrolyte properties and delays the onset of lithium plating.^{22,23} However, the temperature increase must be handled carefully to prevent degradation.¹³ Another option for decreasing the charge time is to maximize the current at all states of charge without reaching the onset of lithium plating or increasing the cell temperature too high. The most common techniques are multi-stage, constant-current, (MCC) charging algorithms, which use insight from separate experiments (*e.g.*, reference electrode measurements, volume expansion data, and post mortem analyses) to design protocols that systematically adjust the current during charging.^{13,27,28} In addition, electrochemical models have been used to further refine the charging protocols. These models have highlighted the importance of using multiple current steps and/or ramping voltages during charging.^{29–33}

The primary control-lever for the fast-charging protocols described in the previous paragraph is the electrical operation of the cell – *i.e.*, applied current/voltage. Several protocols also set an elevated initial temperature as a secondary control.^{29,31} However, the temperature is only set at the beginning of charge and does not supply feedback to the control scheme. For instance, there are no changes in the applied current/voltage or cooling conditions (*i.e.* thermal management) to protect the battery from excessive temperatures during fast charging. This is likely because the above protocols focus on preventing lithium plating, with less concern about thermal degradation. However, limitations on both lithium plating and maximum temperatures should be included into fast-charging protocols to prevent degradation.¹³ This implies that the real limit for fast charging of an EV battery pack will depend on the entire control system: electrical and thermal.

This work seeks to lay the groundwork for developing fast charging protocols by studying the theoretical limits of fast charging using both control systems: electrical and thermal. A constant

risk (CR) charging profile is presented that controls the current to minimize charging time, while maintaining the cell within pre-defined boundaries (i.e., maximum charging current, maximum cell temperature, and minimum overpotential to prevent lithium plating) that constrain the risk of degradation. A continuum-level model of a lithium-ion pouch cell is used to simulate charging with the constant risk profile. These simulations are coupled with three thermal management conditions: adiabatic, constant thermal management, and active thermal management, where the latter incorporates feedback based on the temperature of the cell. These cooling conditions demonstrate ways to use the entire battery management system (electrical and thermal) to control fast charging while preventing degradation. Results, which are based on theoretical calculations and estimated parameter values, should be considered as upper-bounds or best-case scenarios for fast charging within thermal and electrochemical boundaries. This information is incorporated into a battery performance and cost model (i.e., BatPaC: a freely available software from Argonne National Laboratory) to quantify the impact of fast charging requirements on battery cost.³⁴

Model Description

An overview of the model used in this work for a graphite/NMC 532 cell is described in Figure 1. This cell chemistry was selected because it is a commercially available, high-energy cell used in electric vehicles with a significant amount of literature on its thermal and electrochemical properties.^{22,35–37} Details on the model equations, constants, parameters, and solving methodology can be found in the Supplemental Procedures. To summarize, a 3-D thermal model of a stiff pouch cell is coupled with two, 1-D electrochemical models. The 3-D model predicts the temperature distribution in the cell during fast charging. The first electrochemical model (solved at T_{avg}) is used to determine the heat generation rate within the 3-D thermal model and overall

electrochemistry of the cell. The second electrochemical model (solved at T_{min}) is used to predict the onset of lithium plating based on the anode overpotential at the separator-anode interface. This approach reduces calculation times in large-scale simulations compared to fully coupled 3D models, still providing accurate local variables. Its validation to a fully coupled 3D model is presented in the Supplemental Procedures.^{38,39}

The model is used to study the limits of fast charging under thermal and electrical considerations, whereby the model controls the charging current and the coolant flow based on the trajectory of the lithium plating overpotential and the cell temperature. To control the charging current, a constant risk (CR) charging protocol is introduced that maximizes the current within pre-defined, operational limits that minimize the risk of degradation (see Supplemental Procedures for details). These limits are set for the following design variables: *i*) the maximum allowable C-rate to prevent particle fracturing (I_{lim}), *ii*) the maximum allowable temperature to prevent electrolyte decomposition ($T_{max,lim}$), and *iii*) the minimum allowable overpotential to protect against lithium plating in the anode (η_{PP}). At all times, the model operates at the maximum allowable C-rate unless $T_{max,lim}$ or η_{PP} are reached, at which point the current is reduced and/or thermal intervention is employed to minimize the risk of degradation (see next section for details).

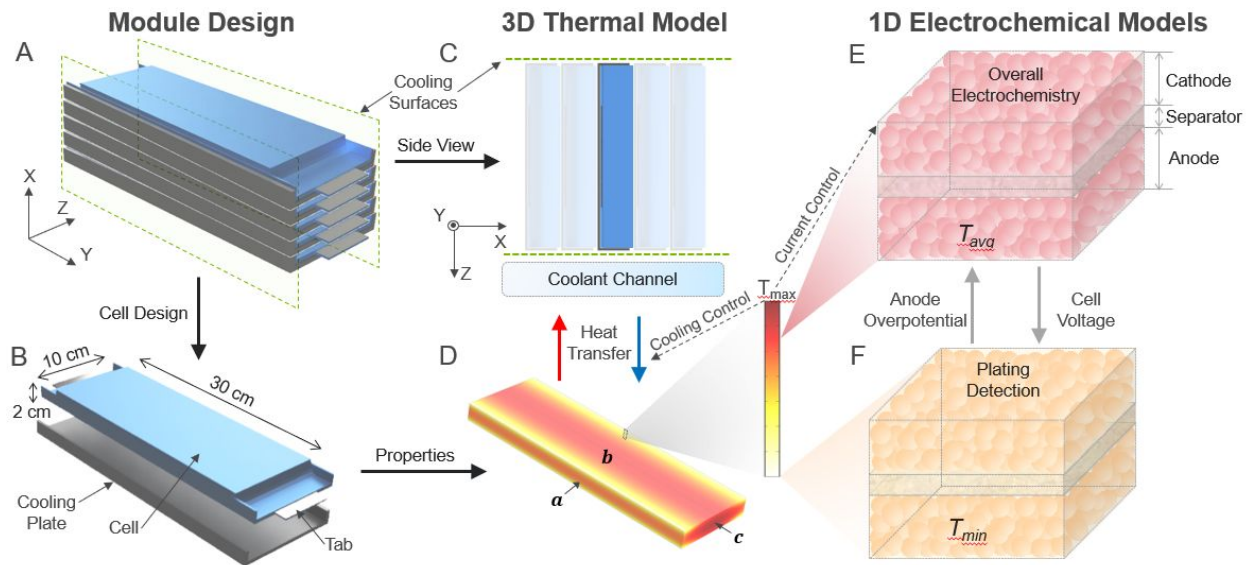


Figure 1. Overview of the electrochemical-thermal model: a 3-D thermal model is coupled with two, 1-D electrochemical models solved at different temperatures within the cell.

(A) CAD rendering of the simulated cells within a battery module.

(B) Rendering of the simulated cell with an aluminum cooling plate. Both components are included in the thermal model. The cell geometry is kept constant for all simulations.

(C) Schematic of the battery module showing the location of the cooling channels along the flanged portion of the aluminum plate. The thermal model accounts for heat transfer between the coolant and the flanges.

(D) Image of the cell during a thermal simulation. Cooling occurs on type-‘*a*’ and type-‘*b*’ faces from contact with the aluminum plate. Type-‘*c*’ faces are assumed adiabatic. T_{avg} and T_{min} from this simulation are used as inputs into the electrochemical models. T_{max} is used as feedback to control the coolant flow and charging current, for applicable cases.

(E, F) Schematics of 1-D electrochemical models solved at (E) T_{avg} and (F) T_{min} in the 3-D cell. Both models have identical structures but are solved at different temperatures. Heat generation

predicted by model in (E) is used as input into 3-D thermal model. The onset of lithium plating predicted by model in (F) is used as feedback to control the charging current.

Results & Discussion

This work starts by analyzing the fast-charging behavior of a Li-ion cell using the CR charging protocol with three possible thermal management strategies: zero (adiabatic), constant (always on), and active (on/off control) (Figure 2). Motivated by the results of this analysis, a detailed study of the constant-risk protocol with active thermal management (CR-ATM) is presented in Figures 3 and 4. Once thoroughly examined, the CR-ATM protocol is used to explore how the cell design (namely electrode loading) and allowable risks of degradation (I_{lim} , $T_{max,lim}$, and η_{PP}) impact the cell's fast-charging time (Figure 5). Finally, work is presented quantifying the impact of fast charging requirements on battery cost (Figure 6).

Optimizing thermal and electrical control strategy

The model was first exercised to simulate the CR charging protocol from 15-95% SOC in combination with three thermal management scenarios: zero thermal management (ZTM), constant thermal management (CTM), and active thermal management (ATM). Figure 2 provides examples of the simulated results, with simulation details reported in the caption. In the Figure, a maximum allowable C-rate (I_{lim}) of 6C was selected to target 10-minute charging times. Additional simulations for all three scenarios with I_{lim} ranging from 2 to 12C can be found in Figures S1 to S3. For all runs, a maximum allowable temperature $T_{max,lim}$ of 55 °C was selected to represent limits for Li-ion cells with standard, carbonate-based electrolytes. A lithium-plating protection overpotential (η_{PP}) of 10 mV was selected to conservatively prevent lithium plating, which

theoretically occurs at <0 mV. η_{PP} should have a margin that reflects uncertainties in model and control tolerances, such as micro-structural inhomogeneities of the risk condition in the presented model.⁴⁰ A 60- μm thick anode and 50- μm thick cathode were selected to represent the mass loading of a typical EV cell. In Figure 2, four illustrative cases are shown:

Case 1. Zero Thermal Management (ZTM) with No Temperature Limit. This case assumes there is no heat transport from the cell system, whereby the system consists of the cell, the aluminum cooling plates, and the static coolant in the coolant channel. The process begins by charging at I_{lim} (Fig. 2C). Without any heat removal, the temperature remains uniform within the cell and continuously rises with time (Figures 2A and 2B). Due to the increased temperature, the ionic resistance in the cell is reduced and the anode never reaches the η_{PP} set to prevent lithium plating (Fig. 2D). Therefore, the cell maintains I_{lim} during the entire charge (Fig. 2C). A similar behavior is observed for I_{lim} up to 8C (Fig. S1). For 10C and 12C, η_{PP} is reached early on during charge ($<20\%$ SOC), which causes the CR protocol to reduce the C-rate, limiting the advantage of charging at higher rates. Note that, because there is no thermal control, the cell exceeds the assumed $T_{max,lim}$ of 55 °C at $\sim 70\%$ SOC according to Fig. 2A, which violates the constant risk protocol and could lead to increased degradation. This behavior occurs for all C-rates above $\sim 4\text{C}$ (Fig. S1A), whereby the overshoot increases with increasing C-rate.

Case 2. Zero Thermal Management (ZTM) Accounting for Maximum Temperature ($T_{max,lim}$). This case is operated under the same adiabatic conditions as Case 1. However, instead of charging at I_{lim} equal to 6C, Case 2 charges the cell at the highest possible C-rate that does NOT cause the cell to surpass $T_{max,lim}$ (Fig. 2A). This corresponds to a charge rate of 4.1C. Like Case 1, the heating of the cell prevents the plating potential from reaching η_{PP} (Fig. 2D). The cell can maintain the 4.1C rate during the entire charge (Fig. 2C).

Case 3. Constant Thermal Management (CTM). Here, the coolant flows through the channel at a constant rate and the heat removal rate is proportional to the temperature difference between the average coolant temperature and the conducting metal wall adjacent to the cell surfaces. As shown in Fig. 2C, the cell is charged at the maximum C-rate of 6C up to ~30% SOC. At ~30% SOC, η_{PP} is reached (Fig. 2D). This triggers the plating protection mode in the CR protocol, whereby the cell is now operated at the highest possible current without causing the potential to dip below η_{PP} (see constant voltage region in Fig. 2D and decaying current in Fig. 2C). The lithium plating potential is reached because the minimum temperature in the cell is ~20 °C (Fig. 2B). Cold temperatures cause sluggish intercalation kinetics, which increase overpotentials at the anode.⁴¹ For instance, η_{PP} is reached in all simulated values of I_{lim} down to 2C (see Fig. S2). Note that, for the 6C example, at the specified coolant flow rate of 6.8 kg/(m²·s), which corresponds to a pack level heat removal of 6 kW, the coolant temperature remains within 16.5 ± 1.5 °C.

Case 4. Active Thermal Management (ATM). In this case, the coolant flow is turned on if/when the temperature at any location in the cell approaches $T_{max,lim}$ to within a specified value ΔT (say 1°C). Conversely, the coolant flow is turned off if/when the maximum temperature in the cell drops to more than ΔT below $T_{max,lim}$. Fig. 2B shows that, in this example, the coolant flow is turned on at ~67% and ~91% SOC and off at ~74% SOC, as indicated by the abrupt changes in the minimum temperature within the cell. This maintains the maximum temperature close to $T_{max,lim}$ (Fig. 2A). On/Off control of the coolant flow maintains a reasonably high temperature at all points in the cell (Fig. 2B), which allows the cell to operate at I_{lim} for most of the charging period (Fig. 2C) without reaching η_{PP} (Fig. 2D). Unlike the other cases, there is a non-negligible constant voltage step, whereby the cell is held at 4.2 V (the upper cutoff voltage) for the final ~5%

SOC (Fig. 2E). Note that, for cases where $I_{lim} > 6C$ (Fig. S3), the achievable current is limited by η_{PP} , causing all cases to have similar charging times (Fig. S3F).

A comparison of the charging times for all four cases is shown in Fig. 2F. For these cases, CTM (Case 3) shows the longest charging time of ~ 18 minutes, due to the need to reduce the C-rate to prevent lithium plating at cold temperatures. The next longest is the ZTM accounting for maximum temperature (Case 2), which has a charging time of ~ 12 minutes. After that, ATM (Case 4) and ZTM with no T limit (Case 1) both have a charging time of 8 minutes. Note that ATM (Case 4) is able to achieve this without causing the temperature to exceed $T_{max,lim}$, while ZTM with no T limit exceeds $T_{max,lim}$ by ~ 10 °C, which violates the CR protocol.

These results produce several important conclusions. First, under adiabatic conditions, the increasing temperatures avoid η_{PP} and recharge of 80% of the cell's capacity in well under 10 minutes can be achieved. However, since excess temperatures negatively affect the cycle life, prudent operation demands changes to the protocol. One method is to reduce I_{lim} to prevent temperature overshoot. However, this increases charge time. Another method is to employ a cooling strategy. In such cases, cell cooling establishes temperature gradients, and the C-rate has to be managed with respect to the coldest point in the cell. As a result, a constant thermal management strategy which continuously cools the cell has significant draw backs due to low local temperatures and increased charging times. An active thermal management strategy which dynamically controls the cooling applied to the cell appears to be the best method for maintaining high C-rates while preventing temperature overshoot during fast charging.

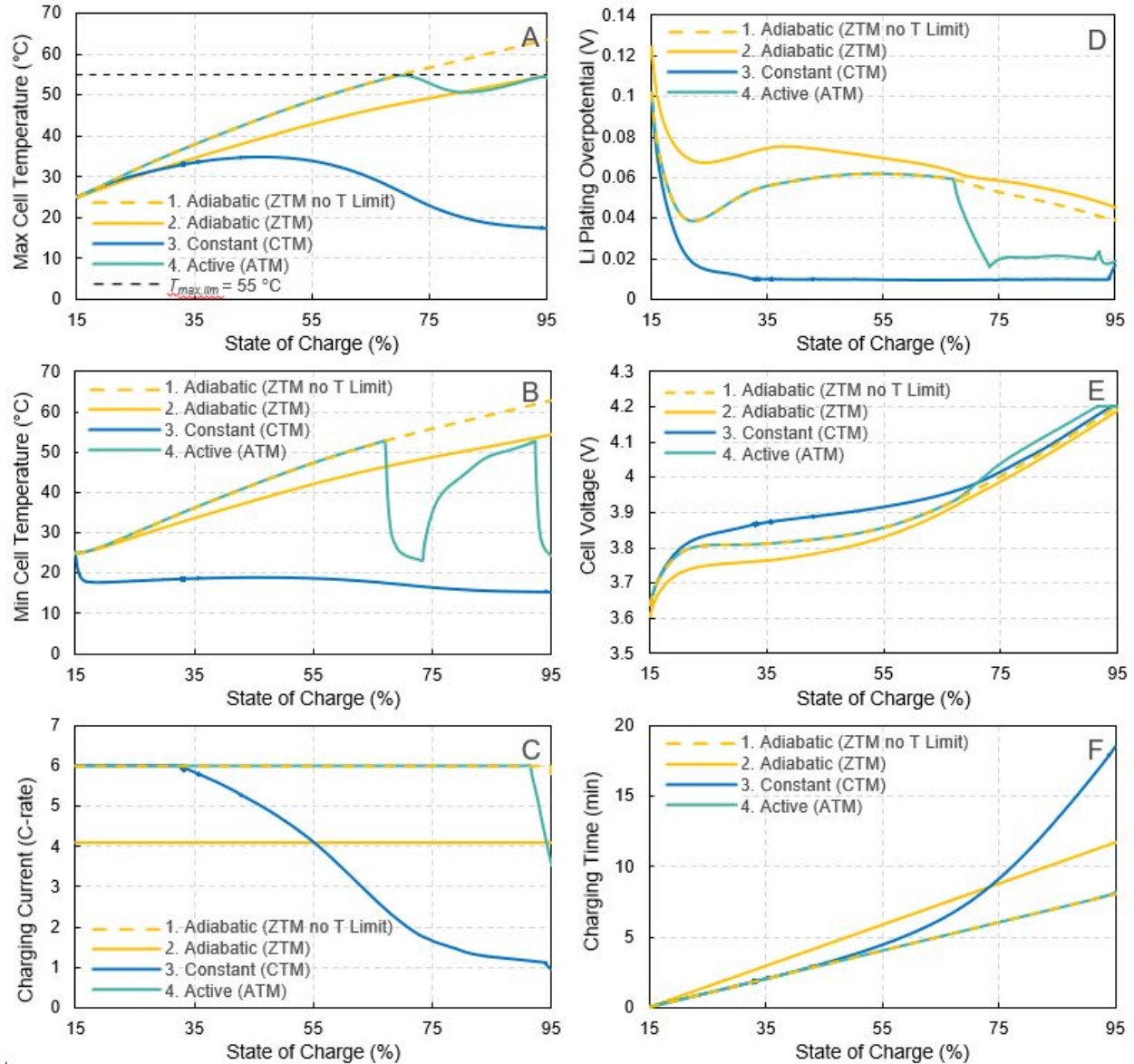


Figure 2. Charging curves for thermal management cases.

(A-B) Maximum and minimum cell temperature from the thermal model.

(C) Charging current reported as C-rate.

(D) Lithium plating overpotential taken at the separator-anode interface from the electrochemical model simulated at T_{min} .

(E) Cell voltage from the electrochemical model simulated at T_{avg} .

(F) Charging time required to charge the cell from 15% to 95% state of charge.

All simulations used an initial temperature (T_0) of 25 °C, a coolant temperature (T_{clnt}) of 15 °C, an overpotential cutoff of 10 mV for lithium plating protection, an upper cutoff voltage of 4.2 V and an anode thickness of 60 μm . The ATM, CTM, and ZTM (no T limit) cases have a maximum charge rate of 6C. The ATM case has a maximum allowable temperature ($T_{max,lim}$) of 55 °C with the coolant flow triggered at 54 °C. The ZTM case (Case 1) has a maximum C-rate of 4.1C, which was the highest allowable C-rate without reaching $T_{max,lim} = 55$ °C.

The above cases suggest that an active thermal management strategy has the potential for fast charging times while also preventing degradation when combined with the CR protocol. To explore this method further, a set of simulations were run with a spread of charging design limits and initial conditions. The graph and table in Figure 3 show charging times and provide descriptions for 20 cases, respectively. The current, temperature, and voltage profiles for each case can be found in Figures S4-S7. For all cases, simulations were operated with a coolant temperature of 15 °C, a maximum C-rate of 6C, and a 60- μm thick anode (50- μm thick cathode). All cells were charged from 15% to 95% SOC using the constant risk protocol. Active thermal management was employed in all cases except A, B, and C, which represented constant thermal management (Case 3 above), zero thermal management accounting for maximum temperature (Case 2 above), and zero thermal management (Case 1 above), respectively. All other relevant conditions for each case are included in the Figure.

Note that conditions D, F, K, O, and Q represent the baseline scenario with active thermal management shown in Figure 2 (Case 4). The first set, “Cooling Method” (A-D), summarizes the results in Figure 2F and clearly reiterates the benefit of active thermal management. The next largest impact on charging time is the maximum allowable temperature ($T_{max,lim}$), whereby

increasing $T_{max,lim}$ from 35 to 55 °C is shown to decrease the charging time from 12.5 to 8 minutes (I-L). Further increases in $T_{max,lim}$ have a negligible impact on charging time because all cells operated with $T_{max,lim} \geq 55$ °C maintain the 6C-rate during charging (Fig. S5). Next, the overpotential cutoff (η_{PP}) (Q-T) has a slight impact, where increasing the overpotential from 10 to 40 mV increases the charging time by ~1 minute. The impact is slight because it only effects the charging current when SOC >75% (Fig. S7). The initial temperature (E-H) is shown to have little impact on the charging time due to the ability of the cell to quickly heat up at the high C-rate used for fast charging (Fig. S4). Note that there is a slight oscillatory relationship between initial temperature and charge time due to the on/off control of the coolant flow (Fig. S9). Interestingly, the temperature that controls when the coolant flow is turned on/off (M-P) has a minimum at 54 °C (or 1 °C below the $T_{max,lim}$). The decrease in charge time from 45 to 54 °C is explained by the benefits of operating the cell at higher temperatures. The increase in charging time from 54 to 55 °C (ΔT from 1 °C to 0 °C) is caused by the constant risk protocol, which reduces the current when $T_{max} > T_{max,lim}$ to prevent overheating (see Figures S6 and S8 for further discussion).

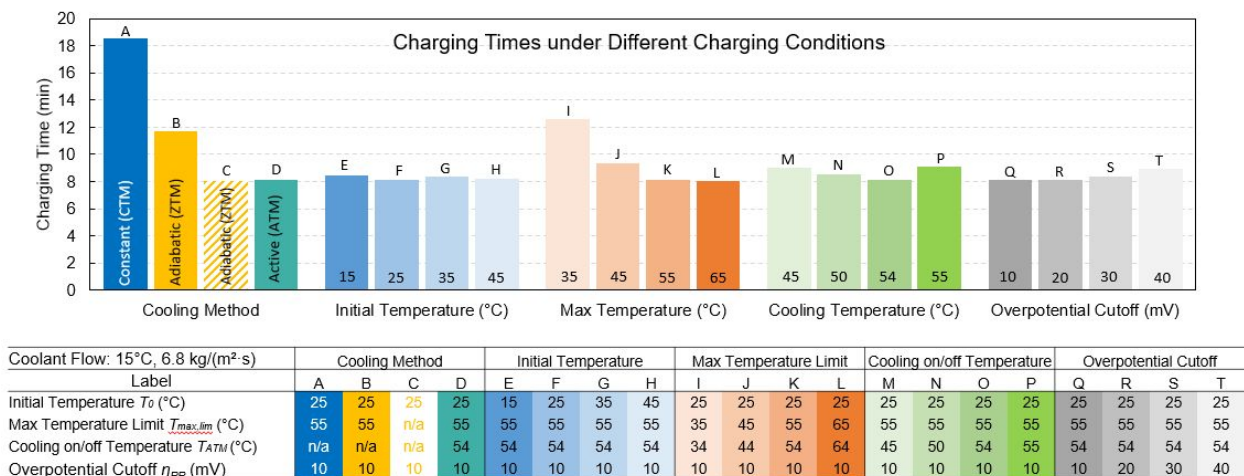


Figure 3. Impact of conditions on charging time.

All simulations were operated with a coolant temperature of 15 °C, a maximum C-rate of 6C, and a 60- μm thick anode. A, B, and C are the only cases not run with ATM. All other relevant conditions are included in the table.

Constant risk charging protocol with active thermal management

A detailed demonstration of the constant risk charging protocol with active thermal management controls was conducted using condition E in Figure 3 (see Figure 4). Condition E was chosen because the 15 °C initial starting temperature ensures the lithium plating protection is triggered in the demonstration. To elaborate, the cell starts at a uniform temperature of 15 °C (Fig. 4D) and is charged at I_{lim} equal to 6C (Fig 4B). During the first ~ 20 seconds, the lithium plating overpotential (measured at the anode-separator interface) drops rapidly due to the high C-rate (Fig. 4B) and moderate temperatures (Fig. 4A). At ~ 20 seconds, the anode reaches η_{PP} (10 mV) and triggers the plating protection mode. From 20 to 100 seconds, the plating protection mode charges the cell at the highest possible current without surpassing η_{PP} . After 100 seconds, the cell reaches and sustains I_{lim} again due to increasing cell temperature.

At time t_1 (~ 6.25 minutes), the maximum temperature in the cell approaches $T_{max,lim}$, which initiates the thermal protection mode and starts the coolant flow. Note that before the coolant is turned on, the temperature in the cell is uniform (the maximum and minimum cell temperature ranged within 2 °C) due to the adiabatic conditions (Fig. 4E). The coolant cools the edge of the cell more rapidly than the inside, which causes a decrease in the anode potential with decreasing T_{min} as shown in Fig. 4C. Fig. 4F shows that the minimum temperature is located at the edge of the cell where there are two contact points with the aluminum conduction plate. At 6.75 minutes, the plating protection mode is triggered again. The thermal protection mode continues until t_2 , when

T_{max} reaches $T_{on/off}$ and cooling is stopped. The cell remains in plating protection mode until ~ 7.8 minutes, when the 4.2 V cutoff is reached, and the constant voltage step is initiated.

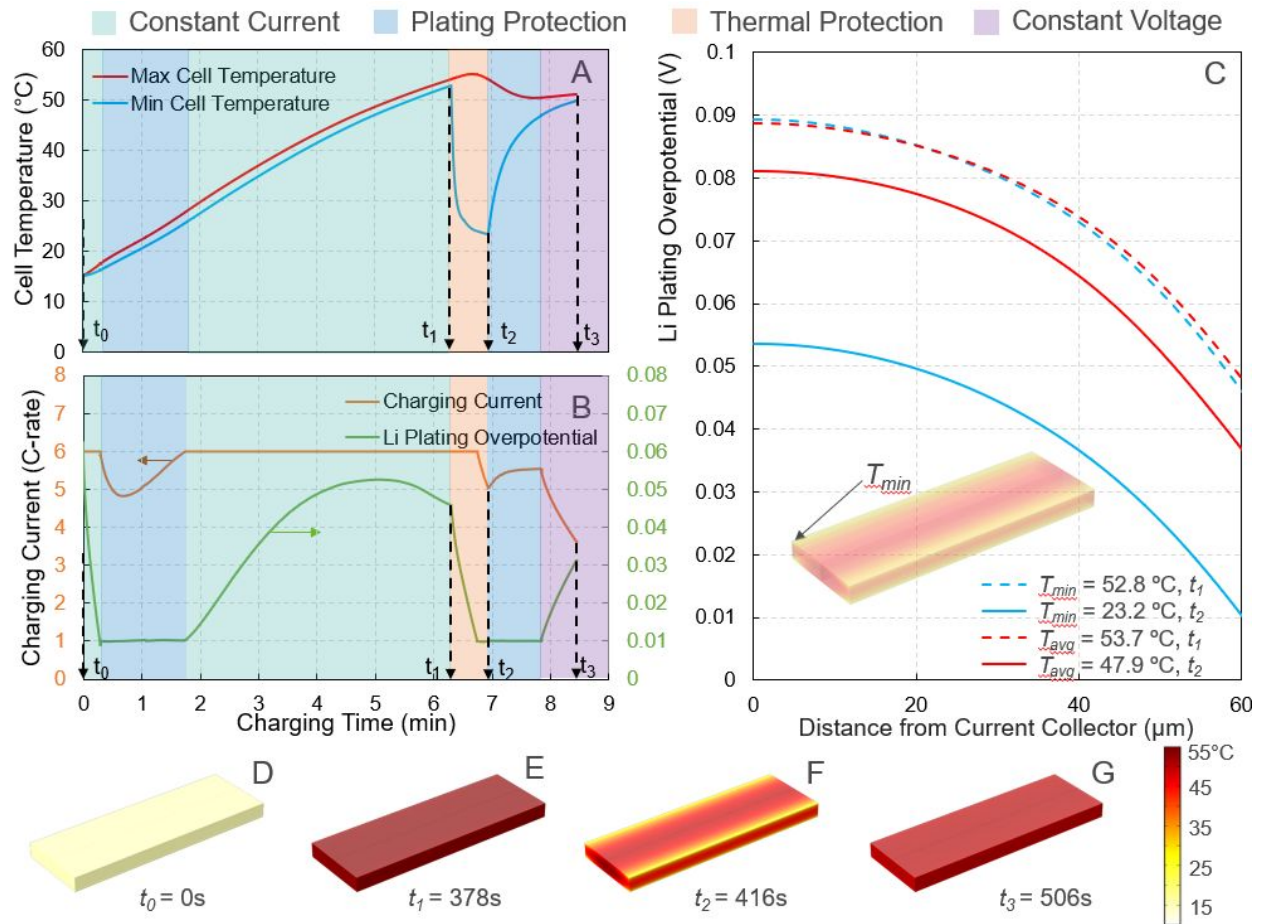


Figure 4. Description of the optimized charging protocol with active thermal management.

(A) Maximum and minimum cell temperature from the thermal model.

(B) Charging current and lithium plating overpotential from the 1-D model at T_{min} .

(C) Lithium plating potential distributions in the anode for both 1-D models at T_{min} and T_{avg} for times t_1 and t_2 .

(D-G) Temperature distribution in the cell at four times during the charging process: start of charging, immediately before coolant flow is started, immediately after coolant flow is stopped, and end of charging.

Simulation uses parameters from condition E in Figure 3.

Charging time dependence on design parameters

Note that the anode thickness, which was set at 60 μm in all previous simulations, directly impacts the charge time since it changes the cell's ability to remain within the three design limits ($T_{max,lim}$, η_{PP} , and I_{lim}) during charge. To explore this concept further, a study was conducted using the model with the CR-ATM protocol to determine the maximum allowable anode thickness that will satisfy a given charge time from 15-95% SOC (Figure 5). All simulations were conducted using a constant cell volume for the 3-D model and a constant anode-to-cathode capacity ratio for the 1-D models. The results were obtained by running a set of simulations at each thickness for a range of I_{lim} (1 to 12 C for Figures 5A-5C) and selecting the minimum charge time within that range. Note that the minimum charge time is typically achieved at several values of I_{lim} within the range since the charge time is often controlled by the other design limits ($T_{max,lim}$ and η_{PP}). For each data point in Fig. 5, the lowest I_{lim} that achieves the same charging time is defined as $I_{lim,min}$, and its value is indicated by the color bar. See Figure S10 for further detail.

Figure 5 demonstrates how “riskier” design limits - *i.e.*, higher $T_{max,lim}$ (Fig. 5A), lower η_{PP} (Fig. 5B), and higher I_{lim} (Fig. 5C) - make it possible for thicker cells to achieve a given charge time. For instance, the inset in Fig. 5A demonstrates that, for a desired 10-minute charge time, increasing $T_{max,lim}$ from 40 $^{\circ}\text{C}$ to 60 $^{\circ}\text{C}$ increases the maximum anode thickness from ~ 60 to ~ 90 μm , which reduces the relative cost ($\$/\text{kWh}$) and increases the energy density of the cell (see

Figures 6 and S11). In Fig. 5B, decreasing η_{PP} from 50 to 10 mV increases the maximum thickness from ~ 65 to ~ 85 μm for a 10-minute charge.

Note that, for these examples, the maximum thickness at 10 minutes is achieved with I_{lim} ranging from 6C to 8C, as indicated by the color of the datapoints. Depending on the cell chemistry, high C-rates can cause particle cracking, which increases degradation. In addition, some C-rates are un-achievable due to charger limitations. Therefore, practical implementation of the CR-ATM protocol may require lowering I_{lim} to account for these factors. To investigate this further, Figure 5C demonstrates how limiting I_{lim} impacts the simulated results. For desired charge times greater than 15 minutes, all five cases (4, 6, 8, 10, and 12C limits) result in the same anode thickness. This arises because, at these times, the maximum thickness is controlled by $T_{max,lim}$ and η_{PP} , which are kept constant for these simulations. At charge times less than 15 minutes, the maximum anode thickness asymptotes at charge times equal to 80% of the constant current charge time because ΔSOC is equal to 80%. For example, when I_{lim} is set to 4C, the charge time is equal to 80% of 15 minutes (*i.e.*, 12 minutes) for all thicknesses below ~ 70 μm . This indicates that cells with sub-70- μm thick electrodes are limited by the C-rate and not $T_{max,lim}$ or η_{PP} in this example.

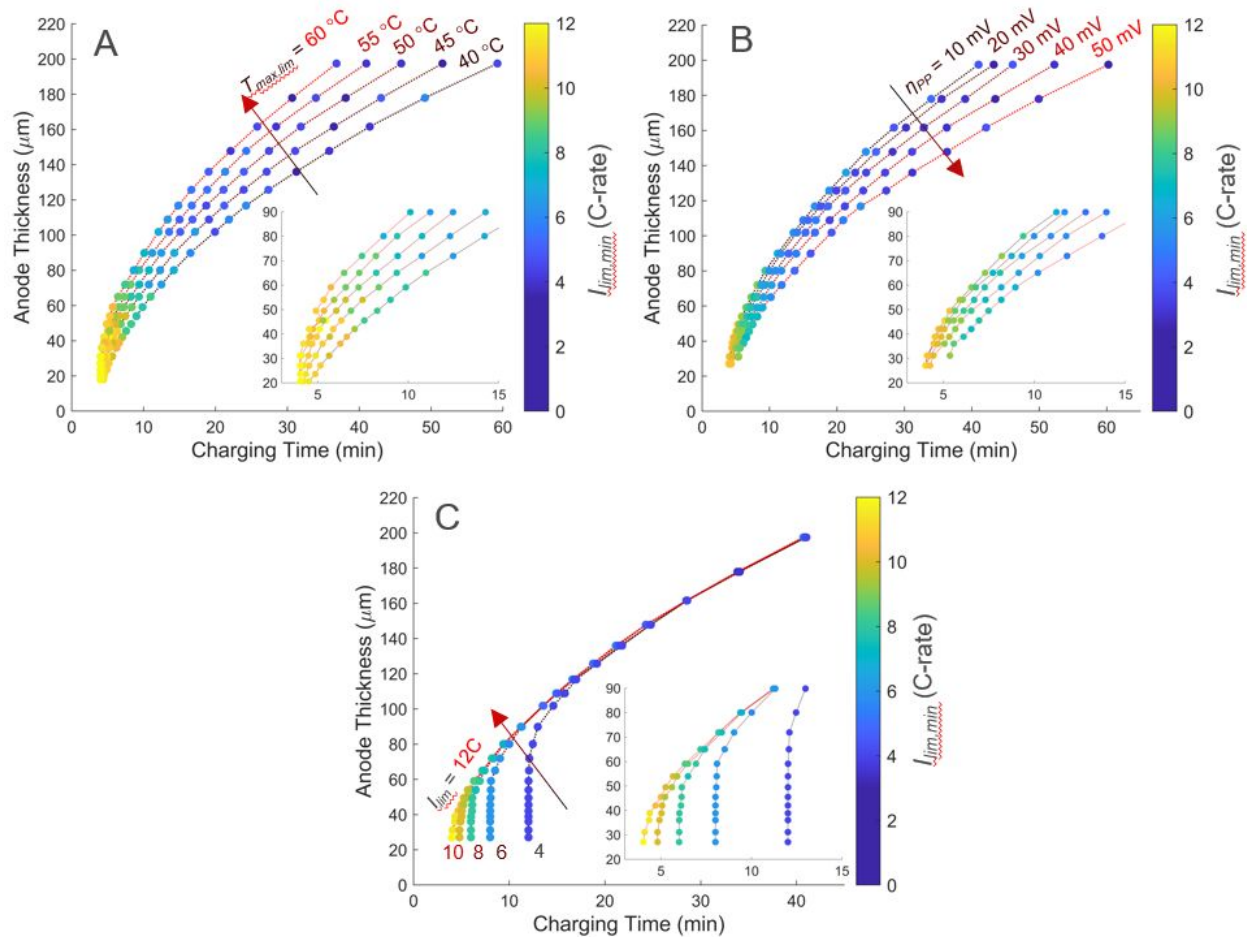


Figure 5. Cell design curves for different charging times and degradation limits.

Maximum achievable anode thickness as a function of charging time and degradation limits using the CR-ATM algorithm. All simulations correspond to charging from 15% to 95% SOC. The color bar provides the value of $I_{lim,min}$, the lowest I_{lim} that achieves the desired charge time at the reported thickness. Insets are zoomed-in data at 2.5 to 15 minutes charge times.

(A) Influence of the maximum allowable temperature ($T_{max,lim}$) in the CR-ATM algorithm on the maximum allowable anode thickness at each charging time. Results obtained from simulations run at $I_{lim} = 2$ to 12C and $\eta_{PP} = 10$ mV.

(B) Impact of decreasing the lithium protection potential (η_{PP}) in the CR-ATM algorithm on charging time. Results obtained from simulations run at $I_{lim} = 2$ to 12C and $T_{max,lim} = 55$ °C.

(C) Effect of the maximum allowable charging current (I_{lim}) in the CR-ATM algorithm on charging time. $\eta_{PP} = 10$ mV and $T_{max,lim} = 55$ °C for all simulations.

Economics of fast charging

One key benefit to maximizing the electrode thickness is it reduces the cost of the cell. Figure 6 summarizes how this can be accomplished by increasing the “riskiness” of the CR-ATM protocol. The figure shows results from three sets of simulations with different CR-ATM conditions, corresponding to safe ($T_{max,lim} = 45$ °C, $I_{lim} = 4$ C-rate, $\eta_{PP} = 30$ mV), moderate ($T_{max,lim} = 55$ °C, $I_{lim} = 6$ C-rate, $\eta_{PP} = 10$ mV), and aggressive ($T_{max,lim} = 60$ °C, $I_{lim} = 12$ C-rate, $\eta_{PP} = 0$ mV) degradation protection limits. Cell costs were determined using the predicted thicknesses and the BatPaC v4.0 software available from Argonne National Laboratory.³¹ See SI section “Battery Cost and Energy Density Modeling” for more detail. For all cases, increasing the desired charge time increases the maximum allowable anode thickness (and cell loading), which decreases the cost. For a 15-minute charge time, the safe, moderate, and aggressive conditions result in 80-, 110-, and 120- μ m thick anodes (3.6, 4.9, and 5.4 mAh cm⁻²) and \$94.5/kWh, \$88.4/kWh, and \$86.6/kWh cells, respectively.

Note that the model predicts more aggressive charge times can only be met by more relaxed operational limits. The safe, moderate, and aggressive conditions have minimum charge times of 12, 8, and 4 minutes due to the restrictions on I_{lim} of 4C, 6C, and 12C, respectively. Also note that the cell cost can rise considerably as the charging limit is approached due to decreases in the electrode thickness. For instance, as the charge time for the moderate conditions decreases from

10 to 9 to 8 minutes, the maximum anode thickness decreases from 80 to 70.8 to 59.8 μm (3.6 to 3.2 to 2.7 mAh cm^{-2}) and the cell costs increase from \$94.2/kWh to \$96.8/kWh to \$102.8/kWh, respectively. This corresponds to a $\sim 9\%$ increase in cost for a two-minute faster charge time.

The results in this study provide useful values for protocol benchmarking, and techno-economic projections. They also provide guidance on the operating conditions a cell must withstand to achieve a desired cost and charging time. For instance, assuming a goal of \$100/kWh for the cell, the simulations show that charging times of 12.8, 8.6, and 6.2 minutes are possible under the safe, moderate, and aggressive CR-ATM protocols, respectively. The rates of degradation associated with these levels of risk are highly dependent on the design decisions made by the cell manufacturer (*e.g.*, electrolyte additives, particle sizes, electrode coatings, and material dopants). Determining the rates of degradation at each level of risk for unique cell designs is outside the scope of this work. In addition, quantifying the “acceptable” rate of degradation, which informs the charging protocol limits, is left for designers to decide on a case-by-case basis depending on their specific cells, consumer-needs (*i.e.*, tradeoff between life and charge time), and pack-design. As more degradation data, which can be tracked with in-situ, measurable, properties (*e.g.*, current, voltage, and temperature), becomes available, the model reported herein can be extended with improved accuracy to aid in these design decisions.

The detailed results of this study are limited to cells with the NMC532/Graphite couple. However, the main conclusions and general trends are expected to apply to next-generation, high-energy, low-cobalt cathodes like NMC811, which are already being implemented in electric vehicles. The conclusions should hold because of similar thermal and electrochemical properties within the layered-oxide family of materials and the fact that lithium plating on the graphite anode is a major factor in determining the charging time. Note that replacing the NMC532 with NMC811

may yield a lower \$/kWh at a given loading by 5-15% in Figure 6 due to the higher energy density of NMC811, although the relative prices of the two materials would be a factor. In addition, if attempting to implement a similar protocol, the charging design limits ($T_{max,lim}$, η_{PP} , and I_{lim}) should be adjusted based on differences in the cells' "acceptable" degradation at a given temperature, current, and voltage window. This is not unique to NMC811, and the protocol limits should be revisited even for different formulations of NMC532, as discussed in the preceding paragraph.

It is important to note that the results herein correspond to practical limits for fast charging since this work assumes feedback control based on accurate, real-time measurement of the internal, local, states of the cell such as η and T_{max} . While this work focuses on the best-case scenario for charging, it is important to note that practical implementation of similar protocols may be feasible. For instance, recent studies demonstrate preliminary in-situ cell sensors that could control the charging based on internal measurements.^{27,42} Reduced-order thermal and electrochemical models in the battery management system (BMS) are another possibility for implementation. These models could control the charging based on estimations of the critical internal variables (*i.e.*, T_{max} , η_{PP} , and local C-rate) from typical BMS readings such as current, voltage, and battery skin and ambient temperatures.⁴³⁻⁴⁵ The protocol design should consider the model estimation errors, and more accurate models supported by experimental measurements will enable a tighter protocol design. As the battery ages, the models would need to be updated to reflect the degradation mechanisms, which would require an additional diagnostic model that incorporates BMS readings over the battery lifetime.

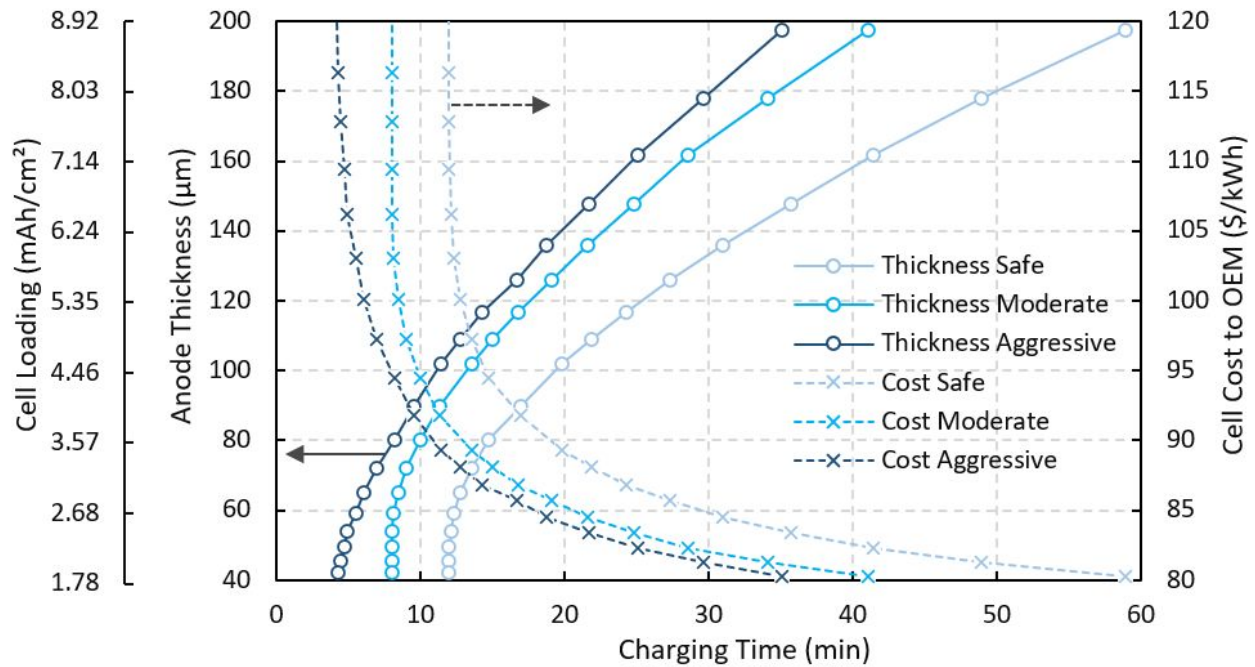


Figure 6. Impact of charging time on anode thickness/loading and cell cost.

Maximum achievable anode thickness/loading and corresponding cell cost as a function of charging time using the CR-ATM protocol. Safe charging conditions correspond to $T_{max,lim} = 45^{\circ}\text{C}$, $I_{lim} = 4\text{C-rate}$, $\eta_{PP} = 30\text{ mV}$; moderate charging corresponds to $T_{max,lim} = 55^{\circ}\text{C}$, $I_{lim} = 6\text{C-rate}$, $\eta_{PP} = 10\text{ mV}$; and aggressive charging corresponds to $T_{max,lim} = 60^{\circ}\text{C}$, $I_{lim} = 12\text{C-rate}$, $\eta_{PP} = 0\text{ mV}$. Charging time determined from 15% to 95% SOC.

Conclusions

This work examined the charging speed limit of Li-ion batteries, by introducing a constant risk charging protocol that maximizes the charging current while maintaining the cell within pre-defined risk of degradation (*i.e.*, maximum allowable temperature to prevent electrolyte degradation, maximum C-rate to prevent particle cracking, and minimum anode potential to prevent lithium plating). When it is paired with an active thermal management (open-loop on/off

control) the constant risk charging protocol provides quicker charging than adiabatic or constant cooling conditions, by quickly escaping the thermal protection mode but still taking advantage of facile transport properties at elevated temperatures (Fig. 2). For a typical NMC/graphite cell with an 80- μm thick anode and a \$90/kWh cell cost, the constant-risk protocol with active thermal management delivers 15-95% charging within 10 minutes (Fig. 4).

This study also elucidated the tradeoff between fast charging time and allowable risks in the protocol design (Fig. 5). For instance, increasing the maximum allowable temperature from 40 to 60 $^{\circ}\text{C}$ can decrease the charging time by up to 50%. Likewise, decreasing the allowable anode potential from 50 to 10 mV can decrease the charging time by up to 35%. Finally, increasing the allowable C-rate from 4C to 12C can decrease the charging time by 67%, but only for thin (<40 μm) anodes where the influence of the other design limits is reduced. These tradeoffs were translated into cell cost curves with respect to the required charging time. More aggressive design limits make it possible to charge thicker electrodes faster, which reduces the cell cost for a given charging target (Fig. 6). For instance, a 12-minute charge time can be achieved for anode thicknesses of 80, 110, and 120 μm , and costs of \$94.5/kWh, \$88.4/kWh and \$86.6/kWh, at relatively safe, moderate, and aggressive protocol designs, respectively. This corresponds to reducing the cell costs from \$94.5/kWh to \$88.4/kWh to \$86.6/kWh.

Author Contributions

J.S. and S.A. developed the research. All authors contributed to refining the approach, analyzing the data, and drawing conclusions. J.S. developed the model. Z.L. and J.S. conducted simulations and generated figures. J.K. performed the cost modeling. K.W.K., Z.L., J.S., J.K., and S.A. wrote the manuscript.

Conflicts of Interests

The authors have no competing interests to report.

Acknowledgments

The authors wish to acknowledge Steve Trask, Alison Dunlop, Bryant Polzin, Andy Jansen, from the Cell Analysis, Modeling, and Prototyping (CAMP) facility and Andrew Colclasure (NREL) for some data sources and information for parameterization; and Gary L. Henriksen, for his help in preparing this manuscript. Support from Brian Cunningham, Samuel Gillard, and David Howell at the Vehicle Technologies Office, Office of Energy Efficiency and Renewable Energy, U.S. Department of Energy, is gratefully acknowledged. Argonne National Laboratory's work was supported by the U.S. Department of Energy, Office of Energy Efficiency and Renewable Energy, Office of Vehicle Technologies under contract DE-AC02-06CH11357.

References

- 1 M. Nicholas and D. Hall, *Lessons learned on early electric vehicle fast-charging deployments*, International Council on Clean Transportation, 2018.
- 2 S. Ahmed, I. Bloom, A. N. Jansen, T. Tanim, E. J. Dufek, A. Pesaran, A. Burnham, R. B. Carlson, F. Dias, K. Hardy, M. Keyser, C. Kreuzer, A. Markel, A. Meintz, C. Michelbacher, M. Mohanpurkar, P. A. Nelson, D. C. Robertson, D. Scofield, M. Shirk, T. Stephens, R. Vijayagopal and J. Zhang, *J. Power Sources*, 2017, **367**, 250–262.
- 3 Y. Liu, Y. Zhu and Y. Cui, *Nat. Energy*, 2019, **4**, 540–550.
- 4 United States Advanced Battery Consortium (USABC), LLC., *USABC Goals for Low-Cost / Fast-Charge Advanced Batteries for EVs - CY 2023*, United States Council for Automotive Research (USCAR), LLC., 2017.
- 5 M. Keyser, A. Pesaran, Q. Li, S. Santhanagopalan, K. Smith, E. Wood, S. Ahmed, I. Bloom, E. Dufek, M. Shirk, A. Meintz, C. Kreuzer, C. Michelbacher, A. Burnham, T. Stephens, J. Francfort, B. Carlson, J. Zhang, R. Vijayagopal, K. Hardy, F. Dias, M. Mohanpurkar, D. Scofield, A. N. Jansen, T. Tanim and A. Markel, *J. Power Sources*, 2017, **367**, 228–236.
- 6 A. Tomaszewska, Z. Chu, X. Feng, S. O’Kane, X. Liu, J. Chen, C. Ji, E. Endler, R. Li, L. Liu, Y. Li, S. Zheng, S. Vetterlein, M. Gao, J. Du, M. Parkes, M. Ouyang, M. Marinescu, G. Offer and B. Wu, *eTransportation*, 2019, **1**, 100011.
- 7 M. Keyser, A. Colclasure, J. Major, K. Fink, S. Santhanagopalan, W. Mai, E. Dufek, S. Lubner, R. Prasher, E. McShane, S. Harris, J. Wan, W. Huang, Y. Cui and M. Toney, *Heat generation concerns associated with extreme fast charging*, National Renewable Energy Lab. (NREL), Golden, CO (United States), 2020.
- 8 P. P. Paul, V. Thampy, C. Cao, H.-G. Steinrück, T. R. Tanim, A. R. Dunlop, E. J. Dufek, S. E. Trask, A. N. Jansen, M. F. Toney and J. N. Weker, *Energy Environ. Sci.*, 2021, **14**, 4979–4988.
- 9 T. Waldmann, M. Wilka, M. Kasper, M. Fleischhammer and M. Wohlfahrt-Mehrens, *J. Power Sources*, 2014, **262**, 129–135.
- 10 D. C. Robertson, L. Flores, A. R. Dunlop, S. E. Trask, F. L. E. Usseglio-Viretta, A. M. Colclasure, Z. Yang and I. Bloom, *Energy Technol.*, 2021, **9**, 2000666.
- 11 M. Broussely, P. Biensan, F. Bonhomme, P. Blanchard, S. Herreyre, K. Nechev and R. J. Staniewicz, *J. Power Sources*, 2005, **146**, 90–96.
- 12 A. Friesen, X. Mönninghoff, M. Börner, J. Haetge, F. M. Schappacher and M. Winter, *J. Power Sources*, 2017, **342**, 88–97.
- 13 J. Sieg, J. Bandlow, T. Mitsch, D. Dragicevic, T. Materna, B. Spier, H. Witzhausen, M. Ecker and D. U. Sauer, *J. Power Sources*, 2019, **427**, 260–270.
- 14 T. C. Bach, S. F. Schuster, E. Fleder, J. Müller, M. J. Brand, H. Lormann, A. Jossen and G. Sextl, *Journal of Energy Storage*, 2016, **5**, 212–223.
- 15 X.-G. Yang, Y. Leng, G. Zhang, S. Ge and C.-Y. Wang, *J. Power Sources*, 2017, **360**, 28–40.
- 16 M. Börner, A. Friesen, M. Grützke, Y. P. Stenzel, G. Brunklaus, J. Haetge, S. Nowak, F. M. Schappacher and M. Winter, *J. Power Sources*, 2017, **342**, 382–392.
- 17 M. Fleischhammer, T. Waldmann, G. Bisle, B.-I. Hogg and M. Wohlfahrt-Mehrens, *J. Power Sources*, 2015, **274**, 432–439.

- 18 D. P. Finegan, A. Quinn, D. S. Wragg, A. M. Colclasure, X. Lu, C. Tan, T. M. M. Heenan, R. Jervis, D. J. L. Brett, S. Das, T. Gao, D. A. Cogswell, M. Z. Bazant, M. Di Michiel, S. Checchia, P. R. Shearing and K. Smith, *Energy Environ. Sci.*, 2020, **13**, 2570–2584.
- 19 A. M. Colclasure, A. R. Dunlop, S. E. Trask, B. J. Polzin, A. N. Jansen and K. Smith, *Journal of The Electrochemical Society*, 2019, 166, A1412–A1424.
- 20 A. Raj, M.-T. F. Rodrigues and D. P. Abraham, *J. Electrochem. Soc.*, 2020, **167**, 120517.
- 21 S. S. Zhang, *InfoMat*, 2020, **2**, 942–949.
- 22 A. M. Colclasure, T. R. Tanim, A. N. Jansen, S. E. Trask, A. R. Dunlop, B. J. Polzin, I. Bloom, D. Robertson, L. Flores, M. Evans, E. J. Dufek and K. Smith, *Electrochim. Acta*, 2020, **337**, 135854.
- 23 M.-T. F. Rodrigues, I. A. Shkrob, A. M. Colclasure and D. P. Abraham, *J. Electrochem. Soc.*, 2020, **167**, 130508.
- 24 A. Mistry, F. L. E. Usseglio-Viretta, A. Colclasure, K. Smith and P. P. Mukherjee, *Journal of the Electrochemical Society*, 2020, **167**, 090542.
- 25 F. L. E. Usseglio-Viretta, W. Mai, A. M. Colclasure, M. Doeff, E. Yi and K. Smith, *Electrochim. Acta*, 2020, **342**, 136034.
- 26 W. Mai, F. L. E. Usseglio-Viretta, A. M. Colclasure and K. Smith, *Electrochim. Acta*, 2020, **341**, 136013.
- 27 M. T. F. Rodrigues, S.-B. Son, A. M. Colclasure, I. A. Shkrob, S. E. Trask, I. D. Bloom and D. P. Abraham, *ACS Appl. Energy Mater.*, DOI:10.1021/acsaem.0c03114.
- 28 F. B. Spingler, W. Wittmann, J. Sturm, B. Rieger and A. Jossen, *J. Power Sources*, 2018, **393**, 152–160.
- 29 M. Xu, R. Wang, B. Reichman and X. Wang, *Journal of Energy Storage*, 2018, **20**, 298–309.
- 30 J. Liang, Y. Gan, W. Song, M. Tan and Y. Li, *Journal of Energy Storage*, 2020, **29**, 101307.
- 31 W. Mai, A. M. Colclasure and K. Smith, *J. Electrochem. Soc.*, 2020, **167**, 080517.
- 32 Y. Yin, Y. Hu, S.-Y. Choe, H. Cho and W. T. Joe, *J. Power Sources*, 2019, **423**, 367–379.
- 33 M. Song and S.-Y. Choe, *J. Power Sources*, 2019, **436**, 226835.
- 34 Paul A. Nelson, Kevin G. Gallagher, Shabbir Ahmed, Dennis W. Dees, Naresh Susarla, Ira D. Bloom, Joseph J. Kubal, Juhyun Song, Zhe Liu, BatPaC (Battery Performance and Cost) Software, <https://www.anl.gov/cse/batpac-model-software>, (accessed 2021).
- 35 D. W. Dees, M.-T. F. Rodrigues, K. Kalaga, S. E. Trask, I. A. Shkrob, D. P. Abraham and A. N. Jansen, *J. Electrochem. Soc.*, 2020, **167**, 120528.
- 36 A. Loges, S. Herberger, P. Seegert and T. Wetzels, *J. Power Sources*, 2016, **336**, 341–350.
- 37 A. Loges, S. Herberger, D. Werner and T. Wetzels, *J. Power Sources*, 2016, **325**, 104–115.
- 38 G.-H. Kim, K. Smith, J. Lawrence-Simon and C. Yang, *J. Electrochem. Soc.*, 2016, **164**, A1076–A1088.
- 39 H.-K. Kim, C.-J. Kim, C.-W. Kim and K.-J. Lee, *Comput. Chem. Eng.*, 2018, **112**, 82–91.
- 40 K. A. Smith, H. Iddir, M. A. Keyser, F. L. Usseglio Viretta, W. Mai, A. Colclasure, S. Santhanagopalan, D. Dees, J. Garcia, S. Ahmad, P. Mukherjee and A. Mistry, *Understanding impact of local heterogeneities during fast charge*, National Renewable Energy Lab. (NREL), Golden, CO (United States), 2019.
- 41 Z. Li, J. Huang, B. Yann Liaw, V. Metzler and J. Zhang, *J. Power Sources*, 2014, **254**, 168–182.
- 42 Y. Zhu, J. Xie, A. Pei, B. Liu, Y. Wu, D. Lin, J. Li, H. Wang, H. Chen, J. Xu, A. Yang, C.-L. Wu, H. Wang, W. Chen and Y. Cui, *Nat. Commun.*, 2019, **10**, 2067.

- 43 W. Sung and C. B. Shin, *Comput. Chem. Eng.*, 2015, **76**, 87–97.
- 44 Y. Gao, C. Zhu, X. Zhang and B. Guo, *Energy*, 2021, **221**, 119688.
- 45 A. Li, M. Ponchant, J. Sturm and A. Jossen, *World Electric Vehicle Journal*, 2020, **11**, 75.